APPLIED PHYSICS

Focus-tunable real-time imaging system based on ultrathin perovskite curved image sensor with hierarchical mesh design

Zeping He[1,2]†, Boning Sun[1]†, Hui Lu[1,2], Xidi Sun[1], Zhangsheng Xu[1,2], Yegang Liang[1], Qiuchun Lu[1], Yang Yu[1], Kaiyu Hu[1], Swapnadeep Poddar[3], Wenqiang Wu[4]*, Wenchao Gao[1]*, Xun Han[5]*, Zhiyong Fan[3]*, Caofeng Pan[1,4,6]*

The human visual system's real-time focus-tunable imaging capability has inspired curved imaging system development. However, curved image sensors mimicking the human retina typically lack tunable curvature to match the curved Petzval surface throughout the focus-tunable range. Here, we propose a focus-tunable real-time curved imaging system based on a tunable-curvature perovskite curved image sensor. Using parylene C film for waterproofing and encapsulation, the ultrathin perovskite curved image sensor with the hierarchical mesh design is demonstrated, which conforms to spherical surfaces of different radii while maintaining mechanical stability during deformation. The image sensor exhibits low detection limit (10 nanowatts per square centimeter) and long-term stable dynamic photoresponse. Combining the image sensor with a tunable lens achieves clear images at different distances via simultaneously adjusting both sensor and lens radii. Furthermore, through integrating image sensor with a readout matrix and wireless data collection component, the real-time imaging system is demonstrated with real-time focus-tunable imaging capabilities.

INTRODUCTION

The visual system is the most crucial tool for humans to perceive information from the external environment (*1*). With its exquisite structure, including an adjustable lens and a curved retina, the human eye can achieve focus-tunable imaging, inspiring the development of bioinspired imaging systems (*2*–*4*). One of the key components of the bioinspired imaging system is the curved image sensor. Compared with the planar image sensor, the curved image sensor adapts to the curved focal plane, which not only improves the image quality, especially in the corners, but also simplifies the optical system (*5*–*9*). Notably, the simple lens forms a strongly curved image surface (known as the Petzval surface), which is precisely matched with the curved image sensor. This configuration eliminates the requirement for optical elements used to correct the focal plane and address issues such as field curvature and vignette. In the focus-tunable imaging system, the curved image surface of the lens changes as the focal length is adjusted. To maintain low aberration images throughout the focus-tunable range, the curvature radius of the curved image sensor needs to be simultaneously changed (note S1). Therefore, variable-curvature image sensors are essential components in focus-tunable imaging systems.

Currently, two main strategies are used for manufacturing curved image sensors. One approach involves the in situ growth of the active materials and fabrication of the image sensors directly on rigid hemispherical substrates (*10*–*16*). The curvature of the curved image sensors obtained by this method is fixed, which limits their application in focus-tunable imaging system. The alternative approach refers to fabricating the image sensor on a planar flexible substrate and subsequently transforming it into a curved form (*17*–*27*). However, the flexible image sensors with large thickness have limited flexibility and can only perform simple bending deformation. The curved Petzval surface is nondevelopable and cannot be matched by simple bending of the flexible devices. Therefore, the devices with good conformity (such as the ultrathin designs) are needed to realize the excellent alignment. In addition, during the transformation process, large stress concentrations are typically generated in the relatively rigid active layer due to the limited stretchability of continuous flexible substrates. Patterning the curved image sensor is a straightforward strategy to endow it with stretchability, while the mesh structural design can also effectively adjust the stress distribution to minimize maximum strain (*19*, *28*–*31*). Thus, combining the ultrathin curved image sensor design with a meshed structure allows the device to achieve superior conformity with the curved Petzval surface while maintaining good mechanical stability, which could be crucial for constructing curved imaging systems with tunable curvature for focus-tunable imaging.

In this work, we developed a focus-tunable real-time curved imaging system to mimic the human visual system, based on an ultrathin perovskite curved image sensor with the hierarchical mesh design. The ultrathin thickness of 5.4 μm allows the device to easily bend into the hemispherical shape, while the soft and narrow interconnects deform to absorb the twist and stretch forces from adjacent pixels, ensuring excellent conformation under different curvature conditions. The image sensor demonstrated good mechanical stability under bending states with a low detection limit of 10 nW cm^{-2}, which is beyond the capabilities of human eye photoreceptor cells. To

[1]CAS Center for Excellence in Nanoscience, Beijing Key Laboratory of Micro-nano Energy and Sensor, Beijing Institute of Nanoenergy and Nanosystems, Chinese Academy of Sciences, Beijing 100083, P. R. China. [2]School of Nanoscience and Technology, University of Chinese Academy of Sciences, Beijing 100049, P. R. China. [3]Department of Electronic and Computer Engineering, The Hong Kong University of Science and Technology, Hong Kong 999077, P. R. China. [4]Institute of Atomic Manufacturing, Beihang University, Beijing 100191, P. R. China. [5]Department of Applied Physics, The Hong Kong Polytechnic University, Hong Kong 999077, P. R. China. [6]International Research Institute for Multidisciplinary Science, Beihang University, Beijing 100191, P. R. China.
*Corresponding author. Email: wuwenqiang@buaa.edu.cn (W.W.); gaowenchao@binn.cas.cn (W.G.); xun-hx.han@polyu.edu.hk (X.H.); eezfan@ust.hk (Z.F.); pancaofeng@buaa.edu.cn (C.P.)
†These authors contributed equally to this work.

mimic the focusing capability of the human eye, a shape-tunable convex lens was integrated with the curved image sensor, allowing coordinated curvature adjustments. Through changing the focal length of the convex lens and the radius of the image sensor, object images with low optical aberration at different distances were achieved. Furthermore, the designed circuit connected the pixels of the curved image sensor to the thin-film transistor readout matrix, enabling the real-time display of captured grayscale images. This curved image sensor design and real-time imaging system provide a method to integrate these optoelectronic devices with commercialized circuits, achieving the function of simulating human visual system.

RESULTS

Design and fabrication of the curved image sensor

The intricate structure of the human visual system enables it to achieve visual accommodation. As shown in Fig. 1A, light passes through the refractive system of the human eye (comprising the cornea, lens, and vitreous body) and is received by the photoreceptor cells on the hemispherical retina. The light signal is then converted into the electrical signal, which is transmitted through the optic nerve and processed in the visual cortex, thus enabling vision (*32*). The lens with changeable shape and the hemispherical retina are the keys to a focus-tunable visual system. The curvature-tunable lens, controlled by the contraction and relaxation of the ciliary muscle, enables light from near or distant object to be focused on the retina (*2*, *33*). The hemispherical retina corresponds to the curved focal plane of the refractive system, which greatly simplifies the complexity of the visual system while achieving low aberration imaging. Inspired by the human visual system, we developed a focus-tunable real-time curved imaging system with visual accommodation. As illustrated in Fig. 1B, the system consists of a tunable lens with adjustable focal length, a curved perovskite image sensor, and a matrix readout system. To achieve focus-tunable imaging with low aberration, the curvature of the curved perovskite image sensor could be adjusted in accordance with the lens to match the focal plane under different focal lengths (*34*, *35*). The captured image then can be read and processed by matrix readout system and uploaded to a terminal device via Bluetooth or wireless fidelity (WIFI) to achieve real-time imaging.

To achieve conformal contact with the hemispherical structure of various curvatures, the image sensor should have excellent flexibility and deformability. The thickness of the device has a notable impact on these properties. Thick devices can only perform simple bending and cannot adequately conform to the hemispherical structures, resulting in additional optical aberrations (Fig. 2A). In contrast, the ultrathin device can conform well to different nondevelopable surfaces, which is conducive to the construction of the curved imaging system. The thickness of the device also affects the strain generated during deformation. As shown in Fig. 2B, finite element analysis (FEA) was performed for the deformation of devices with different thicknesses. The results demonstrate that with the increase in thickness, the average strain of both substrate and active layer of the device increases. In the thick devices, the average strain of the active layer is lower than that of the substrate due to the enhanced strain isolation, while these average strains are very similar in ultrathin structure. Mesh structure is an effective method to enhance the stretchability of flexible electronic devices while optimizing the strain distribution and reducing the strain of the active layer during deformation (*36*, *37*). We proposed a serpentine hierarchical mesh (SHM) structure, which includes the hexagonal pixels containing the active layers, narrow connecting lines along the latitudinal direction forming 120° angles with the pixels to connect them into rings, and wide connecting lines with a serpentine structure along the longitudinal direction to link different pixel rings into a mesh [Fig. 2C(a)]. During deformation, strain is uniformly distributed throughout the mesh through changes in the angles between the narrow connecting lines and pixels, as well as the deformation of the serpentine structure

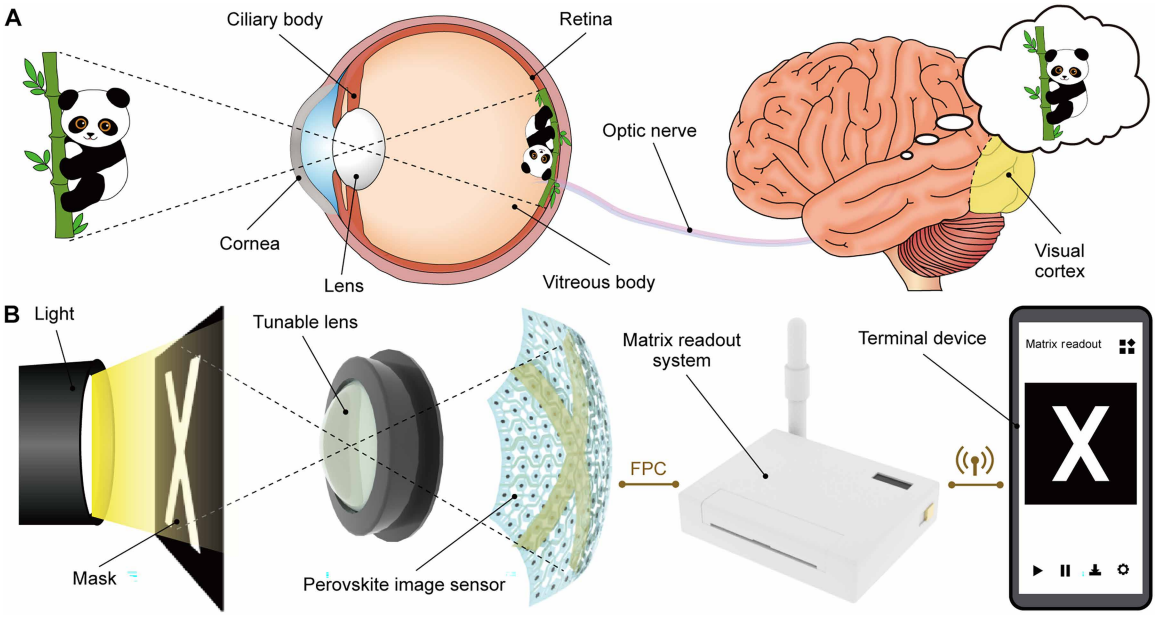

Fig. 1. Overall comparison of the human visual system and the focus-tunable real-time curved imaging system. (**A**) Schematic of the human visual system. (**B**) Schematic of the focus-tunable real-time curved imaging system. FPC, flexible printed circuit.

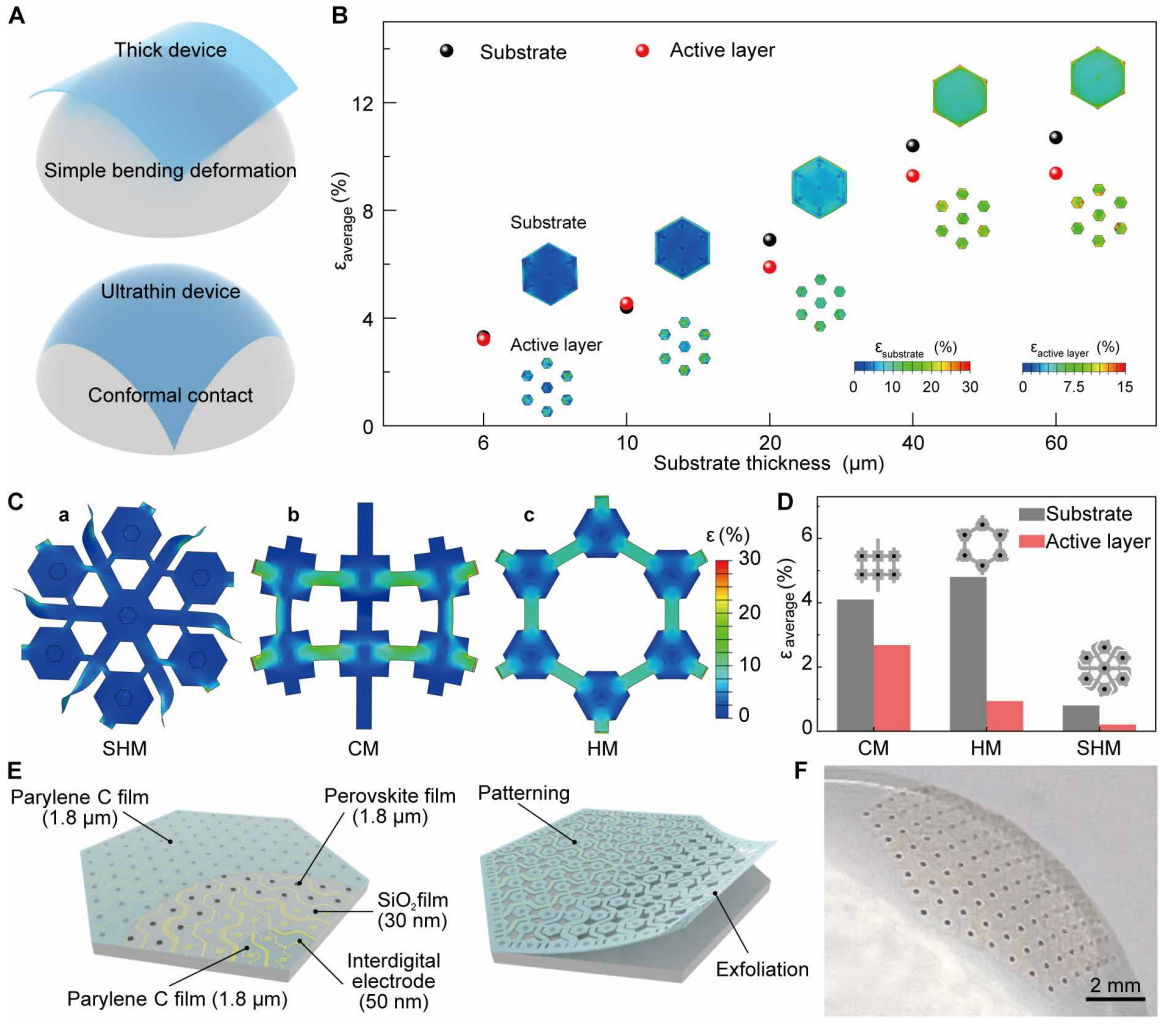

Fig. 2. Design of device structure. (**A**) Schematic diagram of the thick (top) and ultrathin (bottom) devices attached on spherical structures. (**B**) Average strain ($\varepsilon_{average}$) of substrate and active layer obtained by FEA after the devices are deformed into the sphere with a radius of 15.5 mm. (**C**) FEA results of the device with different structures after deformed into the sphere with a radius of 15.5 mm. (**D**) Average strain ($\varepsilon_{average}$) of substrate and active layer obtained by FEA. (**E**) Schematic structure of the ultrathin curved perovskite image sensor with the hierarchical mesh design. (**F**) Optical image of the curved perovskite image sensor attached on a hemispherical surface.

in the longitudinal wide connecting lines (note S2). This design ensures both uniform strain distribution and minimal deformation of the pixels. We compared this structure with common cross mesh (CM) structure and honeycomb mesh (HM) structure. As shown in Fig. 2C [(b) and (c)], when deformation occurs in these two mesh structures, the strain tends to concentrate at the connecting lines and the edges where they join the pixels. Figure 2D demonstrates the finite element analysis results of these three mesh structures with the total thickness of 6 μm under the same deformation conditions. The strains in both substrate and active layer of the SHM structure exhibit notable decrease, confirming its capability to transfer mechanical forces to the uniform small scales (*38*, *39*). Consequently, the ultrathin SHM structure can effectively reduce the possibility of curved image sensor damage during deformation.

The curved image sensors were then fabricated using the ultrathin SHM structure. Figure 2E depicts the structure of the device, which can be divided into five layers. The parylene C film with a thickness of ~1.8 μm was served as the substrate, followed by a 50-nm-thick gold electrode film with an interdigitated structure. A 30-nm-thick SiO_2 film was patterned for selective hydrophobic treatment. The perovskite array, containing 127 pixels with thickness of 1.8 μm, formed the active layer align well with the interdigitated electrodes. Another 1.8-μm-thick parylene C film then encapsulated the entire device to provide good water resistance and flexibility. The cross-sectional schematic of the device is shown in fig. S3, and the overall thickness of the device is ~5.4 μm. To obtain the SHM structure, the device needs further patterning process after encapsulation (Fig. 2E). The detailed fabrication process of the device is illustrated in figs. S4 and S5 (note S3). After patterning, the entire device was effectively transformed into the mesh structure (fig. S6). Then, the ultrathin device was peeled off from the rigid Si support substrate and transformed to the target surface (fig. S6, B and C). Because of its ultrathin and mesh structure, the device can fit well with any shaped curved structure, including the convex surface (Fig. 2F), the three-dimensional (3D) printed concave supports (fig. S6C), and structures with complex surfaces (fig. S7).

Characterization of the perovskite arrays

2D Ruddlesden-Popper (RP) perovskites have a unique layered structure, which results in enhanced stability while maintaining the advantages of low-temperature solution method preparation for flexible substrates (*40*–*42*). 2D RP perovskite $(PEA)_2(MA)_{n-1}Pb_nI_{3n+1}$, where PEA refers to phenylethylammonium, MA refers to methylamine, and $n = 1$, 2, 3, and ∞, was used as the active layer of curved image sensors. The corresponding crystal structure is shown in fig. S8. The bulky organic PEA cation serves as a spacer among the lead halide octahedral planes, forming perovskite layers with different n values. The perovskite arrays with different patterns and arrangements can be achieved through one-step spin coating on patterned substrates (note S4 and fig. S9). The perovskite array demonstrated uniform shape and clear edge with a dense and flat film surface and without the existence of pinholes (fig. S10). Figure S11 shows the x-ray diffraction (XRD) pattern of the perovskite film. The diffraction peaks observed at 14.2° and 28.5° correspond to the (111) and (202) crystal planes of the 2D perovskite, respectively (*43*). Both XRD and scanning electron microscope (SEM) results indicated that the prepared perovskite films have good crystal quality. The optical properties of the $PEA_2MA_3Pb_4I_{13}$ film were characterized using ultraviolet-visible (UV-vis) absorption and photoluminescence (PL) spectra. Distinctive absorption peaks around 514, 564, 603, and 750 nm were observed, corresponding to the $n = 1$, 2, 3, and ∞ phase compositions, respectively (fig. S12) (*44*). PL spectra excited from the front side and back side were collected to characterize the phase composition distribution of the perovskite film in the vertical direction (fig. S13). The front-side PL spectrum exhibited a single emission peak at ~729 nm, emitted by multiple quasi-2D $n > 4$ phases and quasi-3D phases. In contrast, the emission peak of the back-side PL spectrum demonstrated a notable redshift to 743 nm, potentially due to the presence of larger-n phases and efficient transfer of carriers from the low-n to the high-n phases (*45*). Furthermore, the back-side PL spectrum revealed additional emission peaks at around 524, 575, and 615 nm, corresponding to the $n = 1$, 2, and 3 phase compositions, respectively. This suggests a higher concentration of small n ($n \leq 4$) quasi-2D phases at the bottom of the perovskite film. The absorption and PL spectra indicate that the prepared 2D perovskite films have cascade-stacking multidimensional phases from large-n values to small-n values, which is consistent with the literature reports (*43*, *45*, *46*).

Performance and stability of perovskite image sensor

The image sensor arrays were obtained by growing perovskite on the substrate with interdigital electrodes, followed by the encapsulation, patterning, and peeling-off processes. We first characterized the photoresponse of the device after peeling-off and transferring onto a hemispherical structure. As shown in Fig. 3A, there is no notable change in either dark current or photocurrent of the image sensor array, indicating the reliability of patterning and peeling-off process. The photoresponse of an individual pixel was then investigated by the current-voltage (*I-V*) measurement. The *I-V* curves of the device were obtained under 532-nm illumination with different light intensities (Fig. 3B). At 4-V bias, the dark current was ~8 pA, and the output current gradually increased with increasing light intensity. At 10.88 mW cm^{-2}, the output current reached 11.5 nA, corresponding to an on/off ratio of 1.4×10^3. Figure 3C shows the current-time (*I-t*) curves under 4-V bias with different light intensities, exhibiting stable on/off behavior. As shown in Fig. 3D, the device demonstrated reliable photoresponse under both ultraweak (10 nW cm^{-2}) and strong (10.88 mW cm^{-2}) light illumination conditions. Considering that the dark current of the device is ~8 pA, the on/off ratios based on its photoresponse under ultraweak and strong illumination conditions were calculated as 3.5 and 1.8×10^3, respectively. The response time (from 10 to 90%) and decay time (from 90 to 10%) are ~5 and 4 ms, respectively (fig. S14). The intensity-dependent photocurrent ($I_{ph} = I_{light} - I_{dark}$) was calculated from the *I-t* curves and plotted in Fig. 3E (purple curve), fitted by Eq. 1

$$I_{ph} = \alpha P^{\beta} \tag{1}$$

where α is the content, P is the illumination power density, and β is the exponent related to the photoresponse. The fitting value of β is 0.63, indicating a sublinear power-law behavior. Specific detectivity (D^*) is the key index of a photodetector. D^* was calculated according to the Eq. 2 and plotted it in Fig. 3E (blue curve) (*47*)

$$D^* = \frac{I_{ph}}{P\left(2eSI_{dark}\right)^{1/2}} \tag{2}$$

where e, S, and I_{dark} denote the elementary charge, the effective area of an individual pixel, and the dark current, respectively. The maximum D^* was calculated to be 2.3×10^{13} Jones, while the responsivity ($R = I_{ph} / PS$) could reach 3.95 A W^{-1}. Figure 3G presents the *I-t* curve of the device operating continuously for 6 hours under periodic illumination at 10.56 mW cm^{-2}. The performance of the device did not notably decline during long-term operation, demonstrating excellent stable dynamic photoresponse of the photodetector. Furthermore, the device exhibited a wide photoresponse range from 300 to 800 nm (Fig. 3F).

The human eye adjusts its lens shape to focus on objects at different distances (*48*). To simulate this capability of adjusting focus, we used a tunable lens and the curved image sensor to mimic the lens and retina, respectively. Optimal image quality requires simultaneous adjustment of the lens focal length and image sensor radius (R) as the object distance (u) changes (Fig. 4A). For example, at a fixed image distance, both the lens focal length and R decrease as the object approaching. Ray-tracing simulations were used to simulate the curved imaging conditions at varying object distances, generating three imaging conditions ($u = 198$ mm, $R = 17.8$ mm; $d = 108$ mm, $u = 16.8$ mm; $u = 73$ mm, $R = 15.5$ mm). The imaging qualities were then evaluated under these conditions. As illustrated in figs. S15 to S17, the aberration of the image captured by the curved image sensor was less than that of the planar image sensor under identical conditions (note S5).

The mechanical stability of the curved photodetectors array was then characterized to confirm its capability for tunable curvature. Figure 4B shows the photoresponse of device with different bending angles under 532-nm illumination with the light intensity of 10.56 mW cm^{-2}. The optical images of the device under compression and tensile strain are illustrated in fig. S18 (note S6). The device exhibited stable on/off switching response in both upward and downward bending tests due to its ultrathin structure, effective packaging, and hierarchical mesh structure that could avoid stress concentration. Even under the bending state with a large angle of ±100°, the performance of the device was basically unattenuated. To further characterize the mechanical robustness of the device, we tested the *I-t* curves after different bending periods (Fig. 4C). After 2500 bending cycles with an angle of 60°, the device demonstrated a

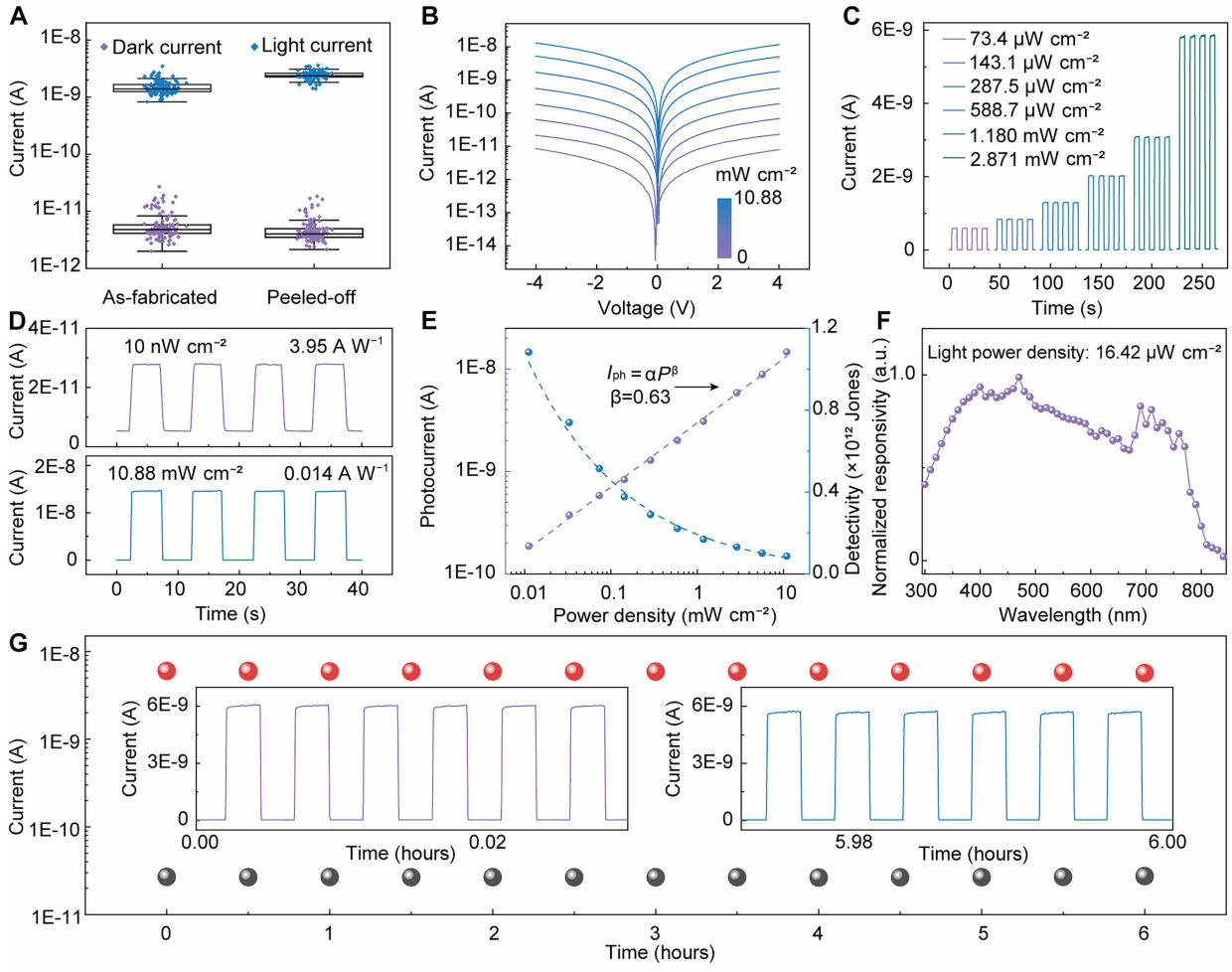

Fig. 3. Optoelectronic performances of the perovskite image sensor arrays. (**A**) Light and dark current statistics of 127 pixels in the device before and after peeling off. (**B**) *I-V* curves of perovskite image sensor arrays in dark and under 532-nm laser illumination with incident light power density ranging from 0 to 10.88 mW cm^{-2}. (**C**) *I-t* curves of image sensor arrays under 532-nm laser illumination with different incident light power density. (**D**) Photoswitching property of the device under illumination with low (10 nW cm^{-2}) and high (10.88 mW cm^{-2}) light power density. (**E**) Dependence of the photocurrent and detectivity on the light intensity. (**F**) Responsivity of device under different wavelengths. a.u., arbitrary units. (**G**) Stability of photodetectors in continuous operation for 6 hours under the bias voltage of 4 V and periodic light with the intensity of 10.56 mW cm^{-2}.

stable response to periodic illumination. The light and dark currents remained basically unchanged compared to the initial state, indicating consistent electrical performance under bending state. The strain of the curved photodetectors array during deformation was analyzed by FEA. Figure 4D shows the strain distribution of the device with hierarchical mesh structure deformed into a sphere with a radius of 17.8 mm. The strain was mainly concentrated on the flexible parylene C substrate, especially in the connection and edge regions. The maximum strain of the substrate is 5.72%, which is smaller than the fracture limit of parylene C (~25%) (*49*). Hexagonal perovskite arrays were strategically placed at the center of the hexagonal parylene C islands to minimize the induced strain on the perovskite, which is identical with the device. FEA results reveal that the maximum strain on the perovskite arrays is 0.13% and the strain in the majority of perovskite film is below 0.1%, notably below the fracture limit of perovskite (~1%) (Fig. 4E) (*50*–*52*). The strain distribution of the devices deformed into spheres with radii of 16.8 and 15.5 mm was also analyzed (fig. S19). Under these two conditions, the strains remained concentrated in the connection and edge regions of the parylene C substrate, with minimal strain in the perovskite layer. While maximum strains on both substrate and perovskite increased as the sphere radius decreased, they remained below their respective fracture limits. Table S1 summarizes the strain behavior of our work with the representative curved image sensors. These results confirm that the hierarchical mesh structure can effectively minimize strain in both the parylene C substrate and the perovskite when deformed into the curved image sensor with different curvatures, ensuring mechanical and electrical stability.

Focus-tunable real-time imaging applications of curved image sensor

To mimic the visual-like imaging system with accommodation, we constructed a real-time imaging system (note S7). As shown in Fig. 5A, the system consists a curved image sensor, a readout matrix, and an image display terminal. A customized flexible circuit board was used to connect and align the pixels of readout matrix with those of the

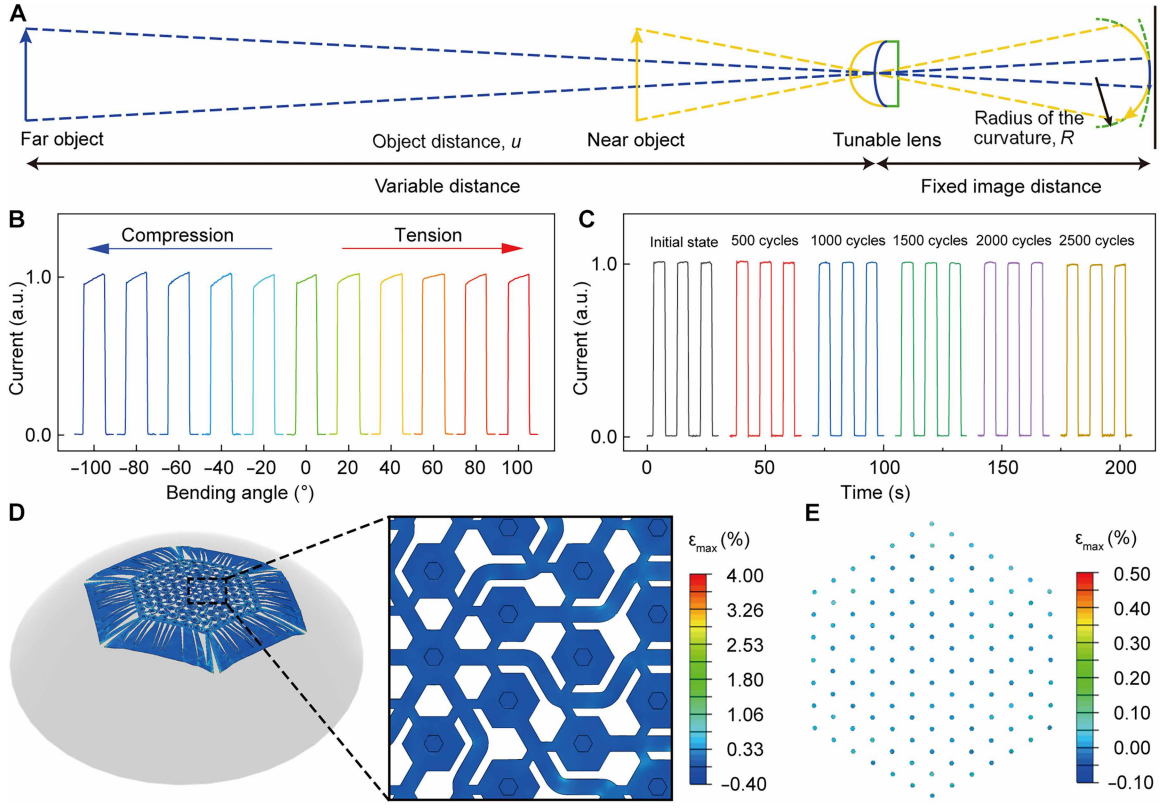

Fig. 4. Deformation of the curved image sensor. (**A**) Schematic diagram of curved image sensor and motorized lens for focus-tunable imaging. (**B**) Photoresponse of the photodetector at a voltage of 4 V with different compression and stretch bending angles and (**C**) after different bending cycles under 532-nm laser illumination with a light power density of 10.05 mW cm^{-2}. [(D) and (E)] FEA results of the (**D**) device and (**E**) perovskite arrays deformed onto a sphere with a radius of 17.8 mm.

curved image sensor. The output current from each pixel of the curved image sensor was obtained by the gate selection and the readout. Subsequently, a field-programmable gate array (FPGA) processed the data and transmitted it to the image display terminal (a mobile phone) via WIFI module for real-time grayscale image display. To focus the light from various distances, we integrated a lens with tunable focal length into the system. External light with shape of "X" was projected onto the tunable lens and then focused on the curved image sensor (Fig. 5B). As illustrated in Fig. 5C, with the object approaching (u = 198, 108, and 73 mm), the focal length of the tunable lens was reduced, and the radius of the curved image sensor also decreased correspondingly (R = 17.8, 16.8, and 15.5 mm) to ensure that a clear X pattern could be obtained. This process fully replicates visual accommodation and, furthermore, adjusts the curvature of the image sensor accordingly to ensure image clarity throughout the entire focal length adjustment process.

This system also demonstrated the dynamic imaging capabilities, where the focal length of the tunable lens was changed while keeping the object distance, image distance, and radius of the curved image sensor constant. As the focal length of the tunable lens decreased from infinity, the image transitioned from blurry (underfocused) to clear (focused) to blurry (overfocused) (Fig. 5D). Consequently, the image of the letter X displayed on the mobile phone underwent a synchronized process (Fig. 5E). Movie S1 recorded the entire imaging process at four times the normal speed. As the focal length of the tunable lens decreased to its minimum and then gradually increased, the letter X in the left area of the movie experienced two changes from blurry to clear to blurry, perfectly corresponding to the image obtained by the imaging system on the right. Movie S2 demonstrated the same process under another imaging condition (u = 108 mm). Movie S3 showed the focus-tunable imaging process with an object distance of 73 mm. Under this condition, because of the limited focal length of the tunable lens, overfocus was not achievable. Therefore, we only observed the letter X gradually becoming clear as the focal length of the lens decreased to the minimum and then becoming blurry again as the focal length increased. The complete real-time image process was illustrated in Movie S4.

DISCUSSION

In summary, we demonstrated an imaging system with the focus-tunable functionality based on the curvature-tunable perovskite image sensor. The ultrathin structure and hierarchical mesh design enable the curved perovskite image sensor to achieve excellent conformality to hemispherical surface with different radii while maintaining mechanical stability during deformation. The utilization of the waterproof parylene C film as both substrate and encapsulation layer endows perovskite devices with uncompromising durability during microfabrication processes including photolithography, patterning, and wet transfer, effectively protecting them from decomposition. By assembling the curved image sensor with a tunable lens and readout matrix, the clear images of objects at different distances

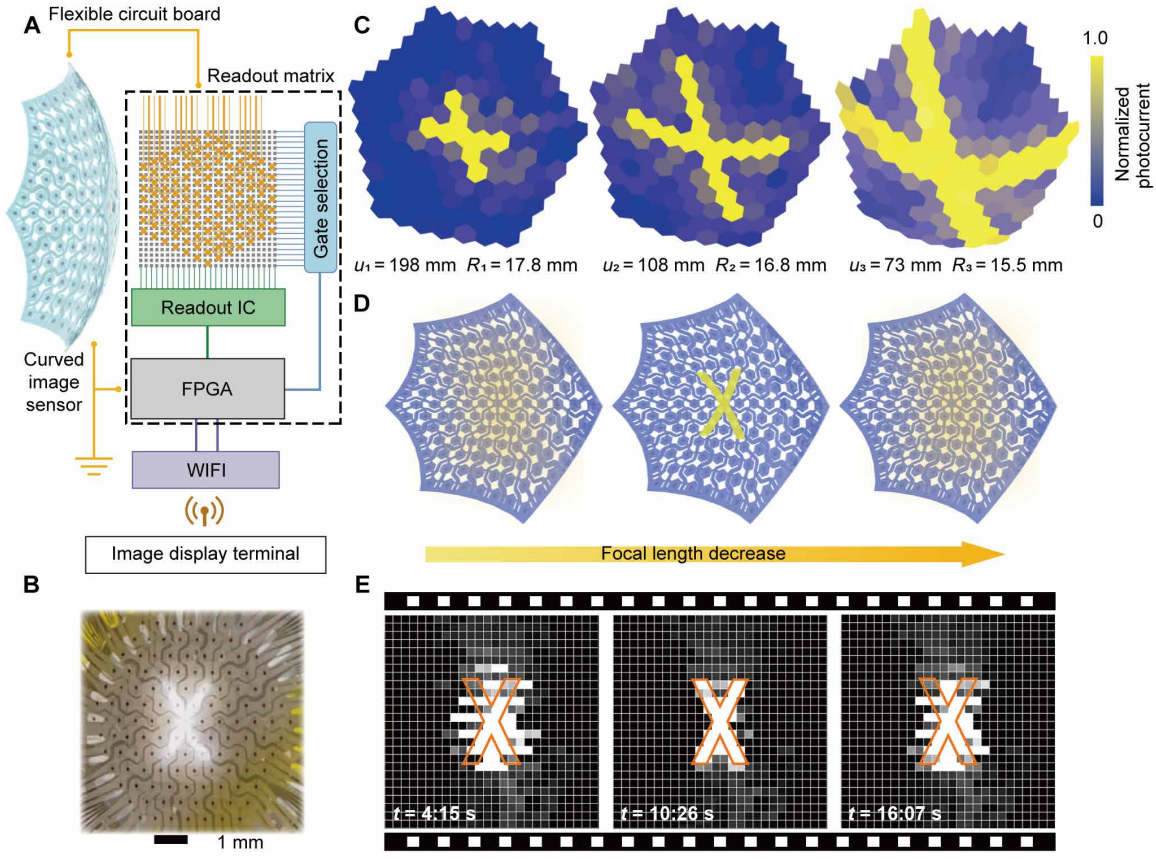

Fig. 5. Demonstration the imaging capabilities of the curved image sensor and the focus-tunable real-time imaging system. (**A**) Circuit schematic diagram of the imaging system integrated with the curved image sensor and a real-time imaging system. IC, integrated circuit. (**B**) The optical photograph in which the letter X is focused on the curved image sensor. (**C**) Imaging results of targets at different distances obtained by the curved image sensor. (**D**) Illustration of the underfocus, focus, and overfocus of the letter X projected on the curved image sensor as the focal length decreased. (**E**) Images acquired by the focus-tunable real-time imaging system at different times during the focal length reduction process.

were captured by adjusting the radius of the lens and the image sensor simultaneously. This function demonstrates its capacity to dynamically adapt its optical configuration and to mimic the visual accommodation, showing its potential for the development advanced bioinspired imaging systems.

MATERIALS AND METHODS

Materials

Phenylethylamine iodide (PEAI; 99.999%), lead iodide (PbI_2; 99.999%), and MA iodide (MAI; 99.5%) were purchased from Xi'an Yuri Solar Co. Ltd. *N*,*N*′-dimethylformamide (DMF; 99.9%) was purchased from Aladdin. 1*H*,1*H*,2*H*,2*H*-perfluorodecyltrimethoxysilane (FAS17; 98%) was purchased from Beijing InnoChem Science & Technology Co. Ltd. All of the chemicals were used as received.

Fabrication of perovskite array

To obtain the patterning perovskite array, the selective hydrophilic/hydrophobic treatment was performed on the substrate. Specifically, the substrate was treated with oxygen plasma (power, 100 W; O_2, 0.2 torr; 300 s) to make it hydrophilic. The photoresist (HTA116 and HTA112, B&C Chemicals) was then used to protect specific areas to maintain hydrophilicity in subsequent processes. The SiO_2 film was deposited on the substrate by magnetron sputtering, and, subsequently, FAS17 was self-assembled on the SiO_2 film to make the surface hydrophobic. The photoresist was removed, resulting in the substrate that was hydrophilic only in certain areas. Then, 60 μl of perovskite precursor was spin-coated on the substrate at 6000 rpm for 40 s, followed by thermal annealing on a hot plate at 100°C for 10 min. The perovskite precursor solution with the concentration of 0.4 M was prepared by mixing PEAI, MAI, and PbI_2 in DMF solution with the molar ratio of 2:3:4 and stirred at 70°C for 3 hours.

Fabrication of curved perovskite image sensor

First, parylene C film was deposited on a p-Si wafer via a polymer organic vapor deposition system [MQP-3001, Maggie Nano Technology (Suzhou) Co. Ltd.]. Then, the designed circuit and electrodes array were obtained by the lift-off process, followed by the perovskite array deposition on the electrodes array. Another 1.8-μm-thick parylene C film was used for encapsulation. Next, the device was patterned by inductively coupled plasma etching with an aluminum film as etching mask. Then, the ultrathin perovskite image sensor was peeled off from the rigid silicon wafer by electrochemical delamination method. Specifically, positive (20 V) and negative (0 V) potentials were applied to the wafer and electrolyte solution, respectively, in 2 M NaCl electrolyte solution. Last, the device was transferred to a 3D-printed curved structure.

Characterizations of perovskite array

The absorption spectrum of $PEA_2MA_3Pb_4I_{13}$ film was characterized by the UV-vis near-infrared spectrophotometer (UV3600). PL spectra were measured by the Edinburgh FLS980. The SEM (Nova NanoSEM 450) was used to characterize the morphologies of perovskite film and cross section of the device. The phase analysis of perovskite film was characterized by x-ray diffractometer (Xpert3 Powder). The step profiler (KLA Tencor P-7 Profiler) was used to measure the thickness of device.

Measurements of curved perovskite image sensor

The photoresponse of the device was characterized by using a 532-nm laser as the light source. The *I-V* and *I-t* curves of the device were tested under dark conditions and different light intensities by current amplifier (Stanford SR570), function generator (Stanford DS345), and a probe station (Semiprobe M-6). The mechanical stability of the device was measured by a stepping motor (LinMot E1100).

Finite element analysis

Finite element analysis was carried out using commercial software ABAQUS2020. The sphere was modeled using eight-node linear bricks with reduced integration and hourglass control, and the flexible substrate and perovskite were modeled using four-node doubly curved thin or thick shells with reduced integration, hourglass control, and finite membrane strains. Finite membrane strains were used to model flexible substrates and perovskite. The meshes of all models were refined sufficiently, and linear elastic models were used. Surface-to-surface contact is used to define the contact between the substrate and the sphere. In the loading configuration, the peripheral edges of the elastic body are constrained along the *z* axis (perpendicular to the substrate plane) while remaining unconstrained in the other spatial dimensions. A z-directional displacement is applied to achieve conformal attachment of the substrate to the curved surface. This displacement parameter maintains load consistency across structural variants in FEA by being uniformly set to 20.6 μm in all 15.5-mm curvature radius simulations.

For regular hexagon substrates, the edge length is 800 μm and the active layer arranged in 2D hexagonal close packing (60-μm hexagonal units with 546-μm interunit spacing). In the HM/CM/SHM structure, active zones are regular hexagons (200-μm edge length) with 100-μm-wide interconnects; the active layer maintains a hexagonal geometry (60-μm edge length) in 2D hexagonal close packing (546-μm lattice spacing). In CM configuration structure, active zones are squares (300-μm edge length) with 100-μm-wide interconnects; the active layer (60-μm edge length) is arranged in 2D tetragonal packing (471-μm grid spacing).

The covered areas were quantified using Image-Pro Plus 6.0 software for statistical analysis. The regular hexagonal substrate demonstrated a total area of 1,667,393 μm^2. The HM architecture substrate exhibited a measured area of 825,641 μm^2. Substrate area for the SM configuration was calculated as 988,436 μm^2. The SHM structural design showed a substrate coverage of 1,095,939 μm^2. CM-type substrates registered a total area of 774,088 μm^2.

Static imaging test of curved image sensor

The tunable lens (EL-3-10, Optotune) was assembled with the curved image sensor, maintaining an image distance of 60 mm. The tunable lens was controlled by a lens driver (electric lens driver 4, Optotune), and the diopter of the lens could be changed by changing the amount of the current. A white light source (LTS-ML70-6-W, LOTS Co. Ltd.) was used to illuminate the Cr mask with the letter X at different locations. A homemade external measurement circuit with a sourcemeter (Keithley 2612B) and a system switch (Keithley 3700A) was used to read out the current data from the imaging sensor. The data were then processed to produce the image pattern.

Real-time imaging test of the imaging system

The curved image sensor was integrated with a real-time imaging system (LZ-03AMR; 64 × 64). With the fast data reading and data processing and the app (MR64) developed by Linkzill, real-time imaging of the curved image sensor was displayed on the mobile phone. In the dynamic focus-tunable test, the current of the tunable lens was increased from 0 to the maximum value, which causes the focal length to change accordingly, so that the image X appeared underfocus, focus, and overfocus.

Supplementary Materials

The PDF file includes:

Notes S1 to S7
Figs. S1 to S22
Table S1
Legends for movies S1 to S4
References

Other Supplementary Material for this manuscript includes the following:

Movies S1 to S4

REFERENCES AND NOTES

1. D. C. D. Pocock, Sight and knowledge. *Trans. Inst. Br. Geogr.* **6**, 385–393 (1981).
2. D. Atchison, *Optics of the Human Eye* (CRC Press, 2023).
3. W. Gao, Z. Xu, X. Han, C. Pan, Recent advances in curved image sensor arrays for bioinspired vision system. *Nano Today* **42**, 101366 (2022).
4. Z. P. He, X. Han, W. Q. Wu, Z. S. Xu, C. F. Pan, Recent advances in bioinspired vision systems with curved imaging structures. *Rare Metals* **43**, 1407–1434 (2024).
5. S. B. Rim, P. B. Catrysse, R. Dinyari, K. C. Y. Huang, P. J. O. e. Peumans, The optical advantages of curved focal plane arrays. *Opt. Express* **16**, 4965–4971 (2008).
6. P. Milojkovic, J. N. Mait, Space-bandwidth scaling for wide field-of-view imaging. *Appl. Optics* **51**, A36–A47 (2012).
7. I. Stamenov, I. P. Agurok, J. E. Ford, Optimization of two-glass monocentric lenses for compact panoramic imagers: General aberration analysis and specific designs. *Appl. Optics* **51**, 7648–7661 (2012).
8. D. Reshidko, J. Sasian, Optical analysis of miniature lenses with curved imaging surfaces. *Appl. Optics* **54**, E216–E223 (2015).
9. B. Guenter, N. Joshi, R. Stoakley, A. Keefe, K. Geary, R. Freeman, J. Hundley, P. Patterson, D. Hammon, G. Herrera, E. Sherman, A. Nowak, R. Schubert, P. Brewer, L. Yang, R. Mott, G. McKnight, Highly curved image sensors: A practical approach for improved optical performance. *Opt. Express* **25**, 13010–13023 (2017).
10. L. Gu, S. Poddar, Y. Lin, Z. Long, D. Zhang, Q. Zhang, L. Shu, X. Qiu, M. Kam, A. Javey, Z. Fan, A biomimetic eye with a hemispherical perovskite nanowire array retina. *Nature* **581**, 278–282 (2020).
11. X. Feng, Y. He, W. Qu, J. Song, W. Pan, M. Tan, B. Yang, H. Wei, Spray-coated perovskite hemispherical photodetector featuring narrow-band and wide-angle imaging. *Nat. Commun.* **13**, 6106 (2022).
12. Z. Long, X. Qiu, C. L. J. Chan, Z. Sun, Z. Yuan, S. Poddar, Y. Zhang, Y. Ding, L. Gu, Y. Zhou, W. Tang, A. K. Srivastava, C. Yu, X. Zou, G. Shen, Z. Fan, A neuromorphic bionic eye with filter-free color vision using hemispherical perovskite nanowire array retina. *Nat. Commun.* **14**, 1972 (2023).
13. S. X. Li, H. Xia, X. C. Sun, Y. An, H. Zhu, H. B. Sun, Curved photodetectors based on perovskite microwire arrays via in situ conformal nanoimprinting. *Adv. Funct. Mater.* **32**, 2202277 (2022).
14. Y. Zhou, Z. Sun, Y. Ding, Z. Yuan, X. Qiu, Y. B. Cao, Z. a. Wan, Z. Long, S. Poddar, S. Kumar, W. Ye, C. L. J. Chan, D. Zhang, B. Ren, Q. Zhang, H.-S. Kwok, M. G. Li, Z. Fan, An ultrawide field-of-view pinhole compound eye using hemispherical nanowire array for robot vision. *Sci. Robot.* **9**, eadi8666 (2024).

15. Y. C. Ding, G. Liu, Z. Long, Y. Zhou, X. Qiu, B. Ren, Q. Zhang, C. Chi, Z. a. Wan, B. Huang, Z. Fan, Uncooled self-powered hemispherical biomimetic pit organ for mid- to long-infrared imaging. *Sci. Adv.* **8**, eabq8432 (2022).
16. X. Feng, C. Li, J. Song, Y. He, W. Qu, W. Li, K. Guo, L. Liu, B. Yang, H. Wei, Differential perovskite hemispherical photodetector for intelligent imaging and location tracking. *Nat. Commun.* **15**, 577 (2024).
17. K. Zhang, Y. H. Jung, S. Mikael, J.-H. Seo, M. Kim, H. Mi, H. Zhou, Z. Xia, W. Zhou, S. Gong, Z. Ma, Origami silicon optoelectronics for hemispherical electronic eye systems. *Nat. Commun.* **8**, 1782 (2017).
18. Y. Chen, Y. Lu, M. Liao, Y. Tian, Q. Liu, C. Gao, X. Yang, C. Shan, 3D solar-blind Ga_2O_3 photodetector array realized via origami method. *Adv. Funct. Mater.* **29**, 1906040 (2019).
19. M. Kim, G. J. Lee, C. Choi, M. S. Kim, M. Lee, S. Liu, K. W. Cho, H. M. Kim, H. Cho, M. K. Choi, N. Lu, Y. M. Song, D.-H. Kim, An aquatic-vision-inspired camera based on a monocentric lens and a silicon nanorod photodiode array. *Nat. Electron.* **3**, 546–553 (2020).
20. Z. Rao, Y. Lu, Z. Li, K. Sim, Z. Ma, J. Xiao, C. Yu, Curvy, shape-adaptive imagers based on printed optoelectronic pixels with a kirigami design. *Nat. Electron.* **4**, 513–521 (2021).
21. E. K. Lee, R. K. Baruah, J. W. Leem, W. Park, B. H. Kim, A. Urbas, Z. Ku, Y. L. Kim, M. A. Alam, C. H. Lee, Fractal web design of a hemispherical photodetector array with organic-dye-sensitized graphene hybrid composites. *Adv. Mater.* **32**, 2004456 (2020).
22. M. Lee, G. J. Lee, H. J. Jang, E. Joh, H. Cho, M. S. Kim, H. M. Kim, K. M. Kang, J. H. Lee, M. Kim, H. Jang, J.-E. Yeo, F. Durand, N. Lu, D.-H. Kim, Y. M. Song, An amphibious artificial vision system with a panoramic visual field. *Nat. Electron.* **5**, 452–459 (2022).
23. M. Kim, S. Chang, M. Kim, J.-E. Yeo, M. S. Kim, G. J. Lee, D.-H. Kim, Y. M. Song, Cuttlefish eye–inspired artificial vision for high-quality imaging under uneven illumination conditions. *Sci. Robot.* **8**, eade4698 (2023).
24. Y. Kim, C. Zhu, W.-Y. Lee, A. Smith, H. Ma, X. Li, D. Son, N. Matsuhisa, J. Kim, W.-G. Bae, S. H. Cho, M.-G. Kim, T. Kurosawa, T. Katsumata, J. W. F. To, J. Y. Oh, S. Paik, S. J. Kim, L. Jin, F. Yan, J. B.-H. Tok, Z. Bao, A hemispherical image sensor array fabricated with organic photomemory transistors. *Adv. Mater.* **35**, e2203541 (2023).
25. W. Lee, Y. Liu, Y. Lee, B. K. Sharma, S. M. Shinde, S. D. Kim, K. Nan, Z. Yan, M. Han, Y. Huang, Y. Zhang, J.-H. Ahn, J. A. Rogers, Two-dimensional materials in functional three-dimensional architectures with applications in photodetection and imaging. *Nat. Commun.* **9**, 1417 (2018).
26. Q. C. Lu, Y. Zhang, G. Yang, M. Xiong, W. Wu, Z. Xu, H. Lu, Y. Liang, Z. He, Y. Yu, X. Mo, X. Han, C. Pan, Large-scale, uniform-patterned $CsCu_2I_3$ films for flexible solar-blind photodetectors array with ultraweak light sensing. *Small Struct.* **19**, 2300364 (2023).
27. W. G. Chung, J. Jang, G. Cui, S. Lee, H. Jeong, H. Kang, H. Seo, S. Kim, E. Kim, J. Lee, S. G. Lee, S. H. Byeon, J.-U. Park, Liquid-metal-based three-dimensional microelectrode arrays integrated with implantable ultrathin retinal prosthesis for vision restoration. *Nat. Nanotechnol.* **19**, 688–697 (2024).
28. R. Jiao, R. Wang, Y. Wang, Y. K. Cheung, X. Chen, X. Wang, Y. Deng, H. Yu, Vertical serpentine interconnect-enabled stretchable and curved electronics. *Microsyst. Nanoeng.* **9**, 149 (2023).
29. K. Sakamoto, H. Kuwae, N. Kobayashi, A. Nobori, S. Shoji, J. Mizuno, Highly flexible transparent electrodes based on mesh-patterned rigid indium tin oxide. *Sci. Rep.* **8**, 2825 (2018).
30. Y. Luo, M. R. Abidian, J.-H. Ahn, D. Akinwande, A. M. Andrews, M. Antonietti, Z. Bao, M. Berggren, C. A. Berkey, C. J. Bettinger, J. Chen, P. Chen, W. Cheng, X. Cheng, S.-J. Choi, A. Chortos, C. Dagdeviren, R. H. Dauskardt, C.-a. Di, M. D. Dickey, X. Duan, A. Facchetti, Z. Fan, Y. Fang, J. Feng, X. Feng, H. Gao, W. Gao, X. Gong, C. F. Guo, X. Guo, M. C. Hartel, Z. He, J. S. Ho, Y. Hu, Q. Huang, Y. Huang, F. Huo, M. M. Hussain, A. Javey, U. Jeong, C. Jiang, X. Jiang, J. Kang, D. Karnaushenko, A. Khademhosseini, D.-H. Kim, I.-D. Kim, D. Kireev, L. Kong, C. Lee, N.-E. Lee, P. S. Lee, T.-W. Lee, F. Li, J. Li, C. Liang, C. T. Lim, Y. Lin, D. J. Lipomi, J. Liu, K. Liu, N. Liu, R. Liu, Y. Liu, Y. Liu, Z. Liu, Z. Liu, X. J. Loh, N. Lu, Z. Lv, S. Magdassi, G. G. Malliaras, N. Matsuhisa, A. Nathan, S. Niu, J. Pan, C. Pang, Q. Pei, H. Peng, D. Qi, H. Ren, J. A. Rogers, A. Rowe, O. G. Schmidt, T. Sekitani, D.-G. Seo, G. Shen, X. Sheng, Q. Shi, T. Someya, Y. Song, E. Stavrinidou, M. Su, X. Sun, K. Takei, X.-M. Tao, B. C. K. Tee, A. V.-Y. Thean, T. Q. Trung, C. Wan, H. Wang, J. Wang, M. Wang, S. Wang, T. Wang, Z. L. Wang, P. S. Weiss, H. Wen, S. Xu, T. Xu, H. Yan, X. Yan, H. Yang, L. Yang, S. Yang, L. Yin, C. Yu, G. Yu, J. Yu, S.-H. Yu, X. Yu, E. Zamburg, H. Zhang, X. Zhang, X. Zhang, X. Zhang, Y. Zhang, Y. Zhang, S. Zhao, X. Zhao, Y. Zheng, Y.-Q. Zheng, Z. Zheng, T. Zhou, B. Zhu, M. Zhu, R. Zhu, Y. Zhu, Y. Zhu, G. Zou, X. Chen, Technology roadmap for flexible sensors. *ACS Nano* **17**, 5211–5295 (2023).
31. S. W. Kim, S. Park, S. Lee, D. Kim, G. Lee, J. Son, K. Cho, Stretchable mesh-patterned organic semiconducting thin films on creased elastomeric substrates. *Adv. Funct. Mater.* **31**, 2010870 (2021).
32. B. Anil, P. Maria, *Next Generation Artificial Vision Systems: Reverse Engineering the Human Visual System* (Artech House, 2008).
33. N. López-Gil, V. Fernández-Sánchez, The change of spherical aberration during accommodation and its effect on the accommodation response. *J. Vis.* **10**, 12 (2010).
34. I. Jung, J. Xiao, V. Malyarchuk, C. Lu, M. Li, Z. Liu, J. Yoon, Y. Huang, J. A. Rogers, Dynamically tunable hemispherical electronic eye camera system with adjustable zoom capability. *Proc. Natl. Acad. Sci. U.S.A.* **108**, 1788–1793 (2011).
35. L. Li, Q.-H. Wang, W. Jiang, Liquid lens with double tunable surfaces for large power tunability and improved optical performance. *J. Opt.* **13**, 115503 (2011).
36. X. Chen, J. Chen, L. Huang, S. Nie, W. Xu, Y. Yin, S. Zhang, F. Pei, K. Yu, W. Su, Y. Wang, W. Yuan, Y. Li, Z. Cui, Highly conductive omnidirectionally stretchable 2D transparent copper mesh electrodes and applications in optoelectronic devices. *Adv. Mater. Technol.* **8**, 2201406 (2023).
37. H. Gao, Z. Wang, F. Yang, X. Wang, S. Wang, Q. Zhang, X. Liu, Y. Sun, J. Kong, J. Yao, Graphene-integrated mesh electronics with converged multifunctionality for tracking multimodal excitation-contraction dynamics in cardiac microtissues. *Nat. Commun.* **15**, 2321 (2024).
38. Z. Yan, Y. Liu, J. Xiong, B. Wang, L. Dai, M. Gao, T. Pan, W. Yang, Y. Lin, Hierarchical serpentine-helix combination for 3D stretchable electronics. *Adv. Mater.* **35**, e2210238 (2023).
39. T. Zhu, K. Wu, Y. Wang, J. Zhang, G. Liu, J. Sun, Highly stable and strain-insensitive metal film conductors via manipulating strain distribution. *Mater. Horiz.* **10**, 5920–5930 (2023).
40. T. L. Leung, I. Ahmad, A. A. Syed, A. M. C. Ng, J. Popović, A. B. Djurišić, Stability of 2D and quasi-2D perovskite materials and devices. *Commun. Mater.* **3**, 63 (2022).
41. I. C. Smith, E. T. Hoke, D. Solis-Ibarra, M. D. McGehee, H. I. Karunadasa, A layered hybrid perovskite solar-cell absorber with enhanced moisture stability. *Angew. Chem. Int. Ed.* **53**, 11232–11235 (2014).
42. Y. Zhou, F. Wang, Y. Cao, J.-P. Wang, H.-H. Fang, M. A. Loi, N. Zhao, C.-P. Wong, Benzylamine-treated wide-bandgap perovskite with high thermal-photostability and photovoltaic performance. *Adv. Energy Mater.* **7**, 1701048 (2017).
43. L. Min, W. Tian, F. Cao, J. Guo, L. Li, 2D Ruddlesden–Popper perovskite with ordered phase distribution for high-performance self-powered photodetectors. *Adv. Mater.* **33**, e2101714 (2021).
44. J. Hu, I. W. H. Oswald, S. J. Stuard, M. M. Nahid, N. Zhou, O. F. Williams, Z. Guo, L. Yan, H. Hu, Z. Chen, X. Xiao, Y. Lin, Z. Yang, J. Huang, A. M. Moran, H. Ade, J. R. Neilson, W. You, Synthetic control over orientational degeneracy of spacer cations enhances solar cell efficiency in two-dimensional perovskites. *Nat. Commun.* **10**, 1276 (2019).
45. Y. Yan, Y. Yang, M. Liang, M. Abdellah, T. Pullerits, K. Zheng, Z. Liang, Implementing an intermittent spin-coating strategy to enable bottom-up crystallization in layered halide perovskites. *Nat. Commun.* **12**, 6603 (2021).
46. Y. Yan, S. Yu, A. Honarfar, T. Pullerits, K. Zheng, Z. Liang, Benefiting from spontaneously generated 2D/3D bulk-heterojunctions in Ruddlesden–Popper perovskite by incorporation of s-bearing spacer cation. *Adv. Sci.* **6**, 1900548 (2019).
47. Y. Tang, F. Wu, F. Chen, Y. Zhou, P. Wang, M. Long, W. Zhou, Z. Ning, J. He, F. Gong, Z. Zhu, S. Qin, W. Hu, A colloidal-quantum-dot infrared photodiode with high photoconductive gain. *Small* **14**, 1803158 (2018).
48. H. Seo, W. G. Chung, Y. W. Kwon, S. Kim, Y.-M. Hong, W. Park, E. Kim, J. Lee, S. Lee, M. Kim, K. Lim, I. Jeong, H. Song, J.-U. Park, Smart contact lenses as wearable ophthalmic devices for disease monitoring and health management. *Chem. Rev.* **123**, 11488–11558 (2023).
49. N. Jackson, F. Stam, J. O'Brien, L. Kailas, A. Mathewson, C. O'Murchu, Crystallinity and mechanical effects from annealing Parylene thin films. *Thin Solid Films* **603**, 371–376 (2016).
50. D. Liu, D. Luo, A. N. Iqbal, K. W. P. Orr, T. A. S. Doherty, Z.-H. Lu, S. D. Stranks, W. Zhang, Strain analysis and engineering in halide perovskite photovoltaics. *Nat. Mater.* **20**, 1337–1346 (2021).
51. S. Y. Lee, S.-H. Kim, Y. S. Nam, J. C. Yu, S. Lee, D. B. Kim, E. D. Jung, J.-H. Woo, S.-m. Ahn, S. Lee, K.-J. Choi, J.-Y. Kim, M. H. Song, Flexibility of semitransparent perovskite light-emitting diodes investigated by tensile properties of the perovskite layer. *Nano Lett.* **19**, 971–976 (2019).
52. S.-M. Ahn, E. D. Jung, S.-H. Kim, H. Kim, S. Lee, M. H. Song, J.-Y. Kim, Nanomechanical approach for flexibility of organic–inorganic hybrid perovskite solar cells. *Nano Lett.* **19**, 3707–3715 (2019).
53. K. Y. Thai, I. Park, B. J. Kim, A. T. Hoang, Y. Na, C. U. Park, Y. Chae, J. H. Ahn, MoS_2/graphene photodetector array with strain-modulated photoresponse up to the near-infrared regime. *ACS Nano* **15**, 12836–12846 (2021).
54. Y. M. Song, Y. Z. Xie, V. Malyarchuk, J. L. Xiao, I. Jung, K. J. Choi, Z. J. Liu, H. Park, C. F. Lu, R. H. Kim, R. Li, K. B. Crozier, Y. G. Huang, J. A. Rogers, Digital cameras with designs inspired by the arthropod eye. *Nature* **497**, 95–99 (2013).
55. J. K. Song, J. Kim, J. Yoon, J. H. Koo, H. Jung, K. Kang, S. H. Sunwoo, S. Yoo, H. Chang, J. Jo, W. Baek, S. Lee, M. Lee, H. J. Kim, M. Shin, Y. J. Yoo, Y. M. Song, T. Hyeon, D. H. Kim, D. Son, Stretchable colour-sensitive quantum dot nanocomposites for shape-tunable multiplexed phototransistor arrays. *Nat. Nanotechnol.* **17**, 849–856 (2022).

Acknowledgments

Funding: This work was support by the National Natural Science Foundation of China (nos. 52125205, 52250398, 52003101, 52192610, and 62422120 to C.P. and 52203307 to W.G.),

Natural Science Foundation of Beijing (L223006 to W.G.), the Shenzhen Science and Technology Program (KQTD20170810105439418 to C.P.), and the Fundamental Research Funds for the Central Universities. **Author contributions:** X.H., Z.F., and C.P. jointly conceived and supervised the project. Z.H., H.L., and X.S. designed and fabricated the device. B.S. and W.G. performed the finite element analysis. Z.H., Z.X., Y.L., and W.W. prepared and characterized perovskite films. Z.H., Q.L., Y.Y., and K.H. characterized the performance of detectors and completed the curved imaging tests. X.H., Z.H., W.W., and S.P. wrote the paper. All authors discussed the results and commented on the paper. **Competing interests:** The authors declare that they have no competing interests. **Data and materials availability:** All data needed to evaluate the conclusions in this paper are present in the paper and/or the Supplementary Materials.

Submitted 15 February 2025
Accepted 1 August 2025
Published 3 September 2025
10.1126/sciadv.adw7826